Acta Crystallographica Section D
Biological Crystallography
ISSN 0907-4449

Structure determination of a truncated dimeric splicing endonuclease in pseudo-face-centered space group $P2_12_12$

Yanming Zhang and Hong Li*

Department of Chemistry and Biochemistry, Institute of Molecular Biophysics, Florida State University, Tallahassee, FL 32306, USA

Correspondence e-mail: hongli@sb.fsu.edu

Received 19 September 2003
Accepted 22 December 2003

PDB Reference: truncated *A. fulgidus* endonuclease, 1r0v, r1r0vsf.

RNA-splicing endonuclease is responsible for the excision of introns in transfer RNA and archaeal ribosomal RNAs. The archaeal form of the enzyme recognizes a unique RNA motif that consists of two three-nucleotide bulges separated by a four base-paired helix, known as the bulge–helix–bulge (BHB) motif. A crystal structure of the RNA-splicing endonuclease from *Archaeoglobus fulgidus* (AF) has been reported previously at 2.8 Å. A truncated but fully active form of AF endonuclease that lacks the N-terminal domain was expressed and crystallized in an orthorhombic space group with two dimers in the asymmetric unit. The calculated native Patterson map suggests strong pseudo-face-centering characteristics, which lead to incorrect space-group assignment by the autoindexing program. The correct space group was determined to be $P2_12_12$ after reindexing. The structure was solved using molecular replacement and was refined to 2.0 Å. The truncated AF endonuclease structure is essentially identical to the corresponding portion of the wild-type AF endonuclease structure in space group $P4_32_12$ as reported previously, with the exception of loop L9, which differs owing to different crystallographic packing. These results confirm the previously described structural features of dimeric splicing endonuclease.

1. Introduction

Archaeal splicing endonucleases are responsible for the recognition and removal of introns in transfer RNA (tRNA) and ribosomal RNA (rRNA) (Kjems & Garrett, 1991; Abelson *et al.*, 1998). The regions of RNA recognized by the splicing endonuclease at the junctions of all introns and exons form a bulge–helix–bulge motif (BHB) consisting of two three-nucleotide bulges separated by four base pairs. Upon association with a BHB RNA, the splicing endonuclease precisely excises the phosphodiester bonds between the second and the third bulge nucleotides. A separate as yet unidentified enzyme is responsible for ligation of the exons of tRNAs in order to complete the process of maturation. Recently, the BHB motif was also identified to be the site of cleavage in small nucleolar RNA processing (Tang *et al.*, 2002). There are over 500 RNAs estimated to conform to the unique BHB RNA motif that are potential substrates for the splicing endonuclease (Moore, 1999; Marck & Grosjean, 2003). Thus, the splicing endonuclease may have much a wider role in archaeal RNA processing beyond that which is currently known. Given the important function of the splicing endonuclease, it is essential to understand how archaeal splicing endonuclease recognizes the BHB RNA motif and functions as an RNA-cleaving enzyme.

Previous structural studies of archaeal splicing endonucleases without a bound BHB RNA substrate have provided insights into how they bind and cleave the BHB RNA. Crystal structures of the splicing endonucleases from *Methanococcus jannaschii* (MJ; Li *et al.*, 1998) and *Archaeoglobus fulgidus* (AF; Li & Abelson, 2000) have been determined. The MJ endonuclease is a homotetramer ($\alpha4$) and is organized into a dimer of dimers, with one subunit from each dimer participating in the catalytic cleavage reaction (catalytic subunits) and the other subunit acting to place the two catalytic subunits correctly in space *via* their L10 loop sequences (structural subunits; Li *et al.*, 1998). The AF endonuclease belongs to the α_2 homodimeric family of endonucleases, with each monomeric subunit containing two homologous domains (or repeats) compared with the MJ endonuclease subunit. This is a result of gene duplication. The C-terminal domain of AF, or the C-repeat, is the catalytic domain, while the N-terminal domain, or the N-repeat, interacts with the catalytic domain from another subunit, leading to an overall structure similar to that of MJ endonuclease (Abelson *et al.*, 1998). These studies revealed that all archaeal endonucleases form a conserved architecture of dyad symmetry that can interact with the BHB RNA motif satisfactorily.

In an effort towards co-crystallizing AF endonuclease with BHB RNA analogs, we have obtained crystals of a truncated AF endonuclease (AFN) lacking the first 60 amino acids. The AFN enzyme is fully active in RNA-cleavage reactions *in vitro*. We describe here the protein expression, crystallization and structure solution of AFN in a pseudo-face-centered orthorhombic space group. The refined AFN structure at 2.0 Å is compared with that of the wild-type enzyme.

2. Materials and methods

2.1. Crystallization and data collection

The AFN gene was cloned into the pET11b vector (Novagen) and transformed into *Escherichia coli* strain BLR(DE3). AFN was purified using the same procedure as described for the wild-type enzyme (Li & Abelson, 2000). Crystals of AFN were obtained using the hanging-drop method, with each drop containing 1.5 µl 60 mg ml^{-1} AFN and 1.5 µl of a reservoir solution consisting of 100 m*M* sodium cacodylate pH 6.5–6.8, 20 m*M* $(NH_4)_2SO_4$ and 300–400 m*M* CH_3COONa. The best crystals grew to a maximum dimensions of 0.03 × 0.03 × 0.05 mm in approximately 30 d.

Diffraction data from AFN crystals were collected at beamline 5.02 of the Advanced Light Source equipped with a Quantum 315 detector (Area Detector Systems Corporation). AFN crystals were briefly transferred to a cryoprotectant solution consisting of the mother liquor plus an additional 25% glucose and 5% glycerol before being flash-cooled in a liquid-nitrogen stream. Monochromatic diffraction data were collected from a single crystal over a range of 200° with a 1° oscillation step. Data were processed and scaled using the *HKL* suite of programs (Otwinowski & Minor, 1997). Data statistics are summarized in Table 1.

Table 1
Data-collection statistics and crystal parameters.

Values in parentheses are for the highest resolution shell.

Space group	$P2_12_12$
Unit-cell parameters (Å)	a = 128.12, b = 144.15, c = 52.39
V_M (Å^3 Da^{-1})	2.23
Molecules per asymmetric unit	4
Estimated solvent content (%)	37
Resolution range (Å)	20.0–2.0 (2.05–2.0)
No. unique reflections	77465
Redundancy†	3.89 (2.46)
Completeness (%)	90.8 (76.5)
$I/\sigma(I)$	13.1 (4.30)
Fraction of reflections with $I/\sigma(I) > 3$	81% (56%)
R_{merge}‡	0.088 (0.352)

† Average number of observations per reflection. ‡ $R_{merge} = \sum|I_{hkl} - \langle I\rangle|/\sum I_{hkl}$, where I_{hkl} is the observed intensity for reflection hkl and $\langle I\rangle$ is the average intensity over multiple observations of symmetry-related reflections after rejection.

3. Results and discussion

3.1. Structure determination for the orthorhombic crystal form of AFN

Initial indexing using *DENZO* (Otwinowski & Minor, 1997) readily identified the Bravais lattice of AFN crystals to be primitive orthorhombic. The unit-cell parameters were first determined to be a = 52.39, b = 128.12, c = 144.15 Å. Each asymmetric unit probably consists of two dimers of AFN based on the calculated Matthews coefficient, V_M = 2.23 Å^3 Da^{-1}, corresponding to 37% solvent content. In order to identify the non-crystallographic symmetry operation between the two dimers, we computed the self-rotation function and native Patterson maps using the reflections in the resolution range 15–4 Å with the *CNS* program (Brünger *et al.*, 1998). Although the self-rotation showed no significant peaks for twofold symmetry, the native Patterson map showed a strong peak at ($u = \frac{1}{2}$, $v = \frac{1}{2}$, w = 0.0) of 71σ, indicating either a translation symmetry of ($\frac{1}{2}$, $\frac{1}{2}$, 0) or a twofold axis parallel to the c axis passing through ($\frac{1}{2}$, $\frac{1}{2}$, 0). The two molecules related by either non-crystallographic symmetry operation will yield a difference vector at ($\frac{1}{2}$, $\frac{1}{2}$, 0). However, twofold non-crystallographic symmetry was quickly ruled out because the crystal exhibited *C*-face-centering pseudo-symmetry, which resulted in a systematically weak ($h + k$ = odd) zone, particularly at low resolution, supporting the presence of the translation symmetry. The calculated intensity ratios for parity reflections with $h + k$ odd/even are 0.261 (25–5 Å resolution) and 0.663 (25–1.9 Å resolution), respectively (Kleywegt & Jones, 1996), thus strongly implying pseudo-*C*-face-centering. This hampered the identification of the correct space group from examining the axial absences, since those along a^* and b^* may be a result of pseudo-*C*-face-centering rather than screw symmetry. We computed average intensity and error ratios (*SCALEPACK*; Otwinowski & Minor, 1997) for the odd and even axial reflections, respectively, and these values are listed in Table 2. Odd reflections along all three axes appeared to be absent at low resolution, which would correspond to space group $P2_12_12_1$. However, if the absences along a^* and b^* were because of pseudo-*C*-centering only, the space group would be

Table 2
Axial reflection intensity statistics of the data set with original indexing.

	Resolution <5 Å		Resolution 5–2 Å	
*h*00	$h = 2n + 1$	$h = 2n$	$h = 2n + 1$	$h = 2n$
No. of reflections	4	3	6	3
Mean I	228.5	33526.6	2289.35	11361.4
Mean σ	32.38	3505.6	324.03	1713.93
Mean I/σ	4.3	10.4	5.7	3.6
0*k*0	$k = 2n + 1$	$k = 2n$	$k = 2n + 1$	$k = 2n$
No. of reflections	8	7	15	16
Mean I	78.03	38326.8	87.34	8010.92
Mean σ	51.17	3594.07	128.81	646.38
Mean I/σ	1.8	11.7	0.7	6.0
00*l*	$l = 2n + 1$	$l = 2n$	$l = 2n + 1$	$l = 2n$
No. of reflections	9	11	18	14
Mean I	246.46	20701.24	366.64	22984.28
Mean σ	44.54	1511.76	98.22	1702.49
Mean I/σ	4.3	13.7	3.2	7.7

$P222_1$. In situations where the apparent symmetry is a combination of pseudo-*C*-centering and screw axes, any of the primitive orthorhombic space groups containing screw symmetries would be possible.

Given the ambiguity in space-group choices, we tested molecular-replacement solutions in all primitive orthorhombic space groups with the original indexing, using an AF dimer model derived from the previously determined full-length AF endonuclease structure in space group $P4_32_12$ (PDB code 1rlv) as the search probe. Although both rotation and translation functions computed using reflections in the resolution range 15–4 Å showed outstanding peaks in all space groups, structural models from these solutions could not subsequently be refined at high resolutions, indicating an incorrect choice of space group. In addition, data were also reduced to *C*-centering orthorhombic space groups in an attempt to search for a molecular replacement solution at low resolution. Neither space group $C222$ nor $C222_1$ yielded any clear translation solutions that could be subsequently refined.

Re-examination of the axial reflections suggested screw axes along b^* and c^*, but not a^* (Table 2), implying 22_12_1 symmetry. Since $P22_12_1$ is not a standard setting, we reindexed the crystal with the *SCALEPACK* program, using $h^{\rm old} \rightarrow l^{\rm new}$, $k^{\rm old} \rightarrow h^{\rm new}$, $l^{\rm old} \rightarrow k^{\rm new}$, such that the twofold axis is placed along the *c* axis, as in $P2_12_12$. The new unit-cell parameters are $a = 128.12$, $b = 144.15$, $c = 52.39$ Å.

A molecular-replacement solution was searched for using the *AMoRe* program (Navaza, 2001) in the new space group for reflections in the resolution range 4–15 Å. The AFN dimer derived from the previously determined AFF structure (Li & Abelson, 2000) was used as a search model. A correlation coefficient (CC) of 23.8% and an *R* factor of 57.7% were first obtained for a single uniquely defined orientation. A translation function calculated based on the unique rotation solution yielded a unique peak with a CC of 56.3% and an *R* factor of 53.7%, which are slightly better than the next highest solution (CC of 52.6% and *R* factor of 55.9%). The position of the second dimer was determined by carrying out another round of the translational search, fixing one dimer at the position that resulted from the first solution. Surprisingly, the solution from the second search yielded worse *R* (61.7%) and CC values (52.2%), probably because of the slight offset in the location of the second dimer. However, the rigid-body refinement routine in the *AMoRe* program readily improved the CC and *R*-factor values to 69.1 and 39.2%, respectively, suggesting that the rigid-body refinement step was critical to further orient the second molecule. In order to assess the pseudo-centering nature of the correct MR solution, the position of the second AFN dimer of the correct MR solution (shown in brown in Fig. 1) was compared with that related to the first AFN dimer (shown in cyan in Fig. 1) by *C*-centering in the original cell or a pure translation to $(0, \frac{1}{2}, \frac{1}{2})$ in the re-indexed cell (shown in green in Fig. 1). As shown in Fig. 1, the AFN dimer identified as the solution in the second MR search is indeed closely related to that placed at the *C*-center (by 4° rotation).

Figure 1
The pseudo-face-centering feature of the AFN crystal. AFN dimers (cyan and brown) within one asymmetric unit are compared with the position of an AFN dimer placed at the *C*-center of the original cell (green). The brown and green copies of the dimer have nearly identical translations from the cyan copy. However, the brown copy is rotated ∼4° from the green copy.

Table 3
Refinement statistics.

Crystallographic residual factors	
Resolution range (Å)	20.0–2.0 (2.05–2.0)
R† (%)	18.56 (23.3)
R_{free}‡ (%)	22.90 (30.7)
Model information	
No. monomers	4
No. amino-acid residues	976
No. protein atoms	8202
No. water molecules	757
Average atomic B factors (Å^2)	
All protein	21.99
Main chain	20.83
Side chain	23.05
Water molecule	39.38
R.m.s. deviations of the model	
Bond length (Å)	0.008
Bond angle (°)	1.163
B, bonded main chain (Å^2)	0.498
B, bonded side chain (Å^2)	1.808
Ramachandran plot	
Residues in most favored region	818 (90.5%)
Residues in additionally allowed region	73 (8.1%)
Residues in generously allowed region	9 (1.0%)
Residues in disallowed region	4 (0.4%)§

† $R = \sum |F_o - F_c| / \sum |F_o|$, where F_o and F_c are the observed and calculated structure factor, respectively. ‡ The R_{free} set uses 5% randomly selected reflections throughout the resolution range. § The outlier is Asp155 in all four subunits. See discussion in text.

We further examined whether the weak reflection zone owing to pseudo-centering in the correct space group could affect the MR solution in other resolution ranges by performing rotational and translational searches at 3, 4, 5, 6 and 7 Å high-resolution cutoffs. We found that the correct peak in the translation function could be identified as the solution at resolutions higher than 6 Å, but at resolutions lower than 6 Å the correct peak diminished to the noise level (data not shown). This result shows that the pseudo-face-centering feature in the AFN crystal obscured the MR solutions at low resolution but not at high to medium resolutions, consistent with the observed difference in intensity ratios for parity reflections at low and high resolutions.

3.2. Structural refinement

Crystallographic refinement of N-terminal truncated AFN was carried out by iterative cycles of manual model building with the program *XtalView* (McRee, 1999) and automatic refinement with *CNS* (Brünger *et al.*, 1998) and *REFMAC*5 (Murshudov *et al.*, 1999). In *CNS* refinement, rigid-body refinement with data to 3 Å resolution was followed by simulated-annealing refinement using all data. Restricted non-crystallographic symmetry (NCS) was also imposed during *CNS* refinement. Difficult regions with ambiguous densities were remodeled on the basis of the map automatically calculated using the hybrid model as implemented in the program *ARP*/*wARP* (Perrakis *et al.*, 2001). This map is unbiased from initial models and NCS restraints and thus can reveal structural differences between the four AFN subunits. Final runs of refinement for AFN structures were carried out with the *REFMAC*5 program, using all reflections to 2 Å (Murshudov *et al.*, 1999). In order to model the anisotropic movement of domains and to account for anisotropy in the data, rigid-body TLS refinement was applied in which each subunit was divided into four different structural domains (domain 1, 62–134; domain 2, 149–214; domain 3, 215–268; domain 4, 269–305). The inclusion of TLS domains and restrained refinement resulted in a large drop in the free R factor (∼3%) and reduced the B factors for each atom while maintaining excellent stereochemistry of the model. Water molecules were added using the *ARP*/*wARP* automatic solvent-build procedure. The program *XPAND* (G. J. Kleywegt, unpublished work) was used to evaluate the geometry and chemical environment of each water molecule; all water molecules were found to be at sites with a reasonable polar environment. The *WATNCS* program from the *CCP*4 suite (Collaborative Computational Project, Number 4, 1994) was used to assess NCS-related water molecules. Of the 757 water

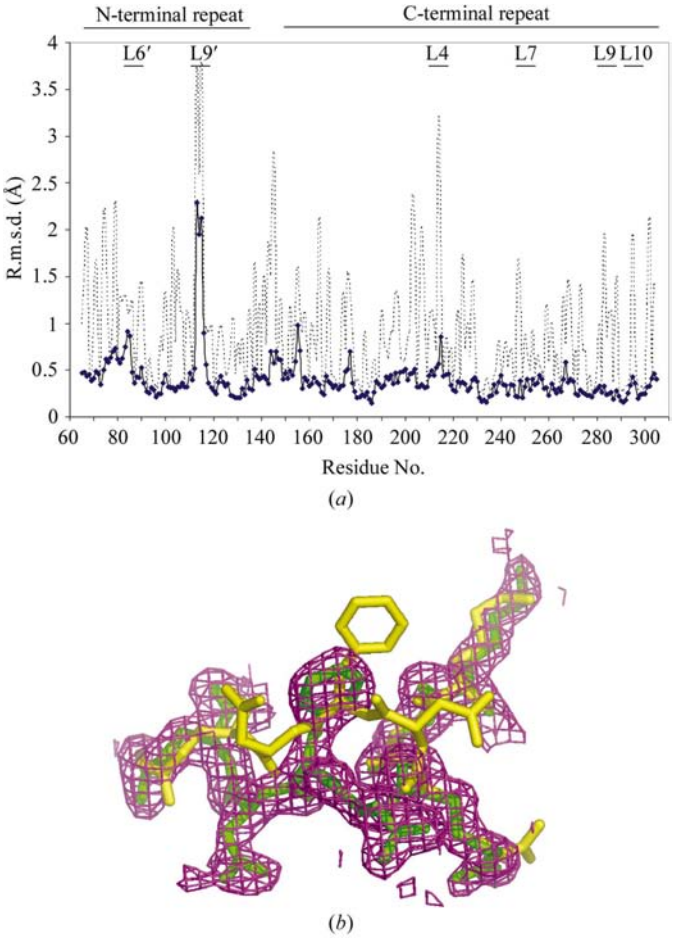

Figure 2
Structural comparison between AFN and AFF $P4_32_12$. (*a*) Averaged r.m.s. deviations per residue between the two structures are displayed as a function of the residue number. The solid lines are for main-chain atoms and the dashed lines are for side-chain atoms. The positions of several loops are indicated with the nomenclature used by Li & Abelson (2000). The large deviation for the loop L9′ (residues 110–115) arises from the unique crystallographic packing in the AFN structure. (*b*) σ_A-weighted $2F_o - F_c$ map around the region of L9′, displayed at the 1σ level, together with the refined AFN model (green) and the initial MR search model (yellow).

molecules, 280 molecules satisfy all the NCS operations and 93 molecules satisfy two NCS operations. The final models were refined to R_{cryst} and R_{free} factors of 18.56 and 22.90%, respectively. Detailed refinement statistics are summarized in Table 3. The final models were analyzed using *PROCHECK* (Laskowski *et al.*, 1993) and were found to be consistent with correct structures.

3.3. Electron density at the proposed catalytic triad

The site of catalysis on the endonuclease is currently unproven because of the lack of co-crystal structures between the endonuclease and RNA substrate. Several lines of evidence suggest that His257 has critical importance in catalysis. This histidine residue is conserved throughout evolution. Its mutation in both archaeal and yeast endonucleases greatly impaired splicing activity (Lykke-Andersen & Garrett, 1997; Trotta *et al.*, 1997). In the previously determined AF and MJ endonuclease structures, this histidine is in close proximity to two other strictly conserved residues, Lys287 and Tyr246. In the center of the three residues of both structures, a region of electron density was identified that could be attributed to a bound SO_4^{2-} ion on the basis of the immediate positive surroundings (Li *et al.*, 1998; Li & Abelson, 2000). This bound sulfate ion was proposed to mimic the binding of a phosphate group on the RNA substrate. A cluster of electron density in the $F_o - F_c$ maps could also be found at the same site in the AFN structure presented here (data not shown), thus further supporting the presence of an anionic group at this site. Definite proof of the chemical identity that resulted in the difference electron density requires additional structural and biochemical studies.

The proposal that the conserved His257 is the active-site residue implies that the cavity lined with loops L7 (where His257 is located), L6 and L9 would be the site of bulge nucleotide binding. In agreement with this hypothesis, this cavity is heavily hydrated in the refined AFN structure (data not shown), suggesting a polar environment that is favorable for nucleic acid binding.

3.4. Structure comparison yielded identical splicing endonuclease fold

The AFN endonuclease structure determined here superimposes well with that reported previously of the full-length AF endonuclease in space group $P4_32_12$ (AFF $P4_32_12$; PDB code 1rlv) (Fig. 2*a*). The overall r.m.s. deviation between the AFF $P4_32_12$ main chain and that of AFN is 0.51 Å. The largest difference was seen in a region that participates in crystallographic packing. Residues 110–115 in AFN significantly deviate from those in the AFF $P4_32_12$ structure (Fig. 2*b*). Another difference between the AFF $P4_32_12$ structure and the AFN structure occurs at residue Asp155. The torsion angles around the Asp155 peptide bond fall outside the allowed regions in the Ramachandran plot (φ = 62.1°, ψ = −100.7°). However, it is obvious that this geometry is consistent with the electron density (Fig. 3). Examination of the Asp155 environment revealed that the unfavorable rotation of the carbonyl carbon–oxygen bond of Asp155 was a result of the truncation of the first 60 amino acids. In the truncated AFN structure, the N-terminal residues 62–64 are no longer anchored by the upstream β-strand available in the full-length protein. Asp155 participates in stabilizing the otherwise unstable N-terminus by forming a polar hydrogen bond with the amide group of Phe63 (Fig. 3). This interaction exerts a steric strain on the main-chain geometry of Asp155, which is subsequently stabilized by the guanidinium group of the nearby Arg208. This structural rearrangement demonstrated a limited flexibility in the AF endonuclease in response to local environment change. Therefore, the unusual backbone geometry of Asp155 was a structural consequence of truncating the first 60 amino acids, rather than a general feature required for endonuclease function.

4. Conclusion

We have described the structure-determination process of a truncated AF endonuclease in a pseudo-face-centered space group using molecular replacement. The N-terminal truncation mutant of AF endonuclease was crystallized in space group $P2_12_12$ with low solvent content. The pseudo-face-

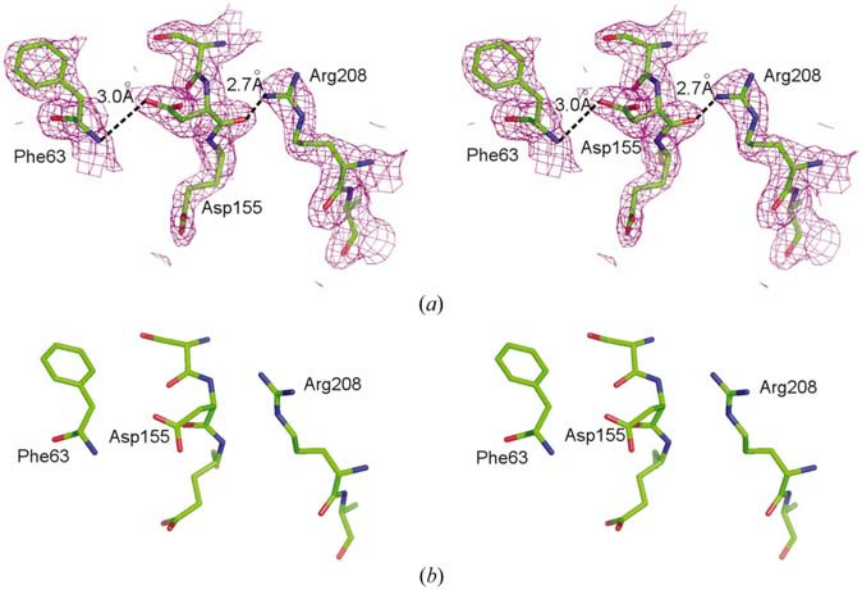

Figure 3
The unusual peptide-bond geometry of Asp155. (*a*) The $2F_o - F_c$ map (1σ) is superimposed on the final refined model of the AFN structure centered around Asp155. As a result of truncation, the N-terminal residues of AFN are no longer stabilized by its upstream β-strand. Additional interactions are formed, such as that between Phe63 and Asp155. This interaction creates an unusual backbone torsion angle that is subsequently stabilized by a polar hydrogen bond formed between the carbonyl O atom and the guanidinium group of Arg208. (*b*) The same residues in the full-length AF endonuclease structure (PDB code 1rlv), displayed with the same orientation; the two close contacts observed in the AFN structure are not observed.

centering made space-group determination less straightforward. The molecular-replacement solution was obtained when the correct space group was determined.

The high-resolution structure of AFN showed structural features similar to those observed in the previously determined full-length enzyme at medium resolution. These include the possible phosphate-binding site in the proposed active site and the mode of oligomerization in the dimeric splicing endonuclease.

This work was supported by a Florida Biomedical Program grant (BM002 to HL). The authors thank Dr J. Abelson for providing support during the initiation of this work and the members of the Li group for helpful discussions.

References

Abelson, J., Trotta, C. R. & Li, H. (1998). *J. Biol. Chem.* **273**, 12685–12688.

Brünger, A. T., Adams, P. D., Clore, G. M., DeLano, W. L., Gros, P., Grosse-Kunstleve, R. W., Jiang, J.-S., Kuszewski, J., Nilges, M., Pannu, N. S., Read, R. J., Rice, L. M., Simonson, T. & Warren, G. L. (1998). *Acta Cryst.* D**54**, 905–921.

Collaborative Computational Project, Number 4 (1994). *Acta Cryst.* D**50**, 760–763.

Kjems, J. & Garrett, R. A. (1991). *Proc Natl Acad. Sci. USA*, **88**, 439–443.

Kleywegt, G. J. & Jones, T. A. (1996). *Acta Cryst.* D**52**, 826–828.

Laskowski, R. A., MacArthur, M. W., Moss, D. S. & Thornton, J. M. (1993). *J. Appl. Cryst.* **26**, 283–291.

Li, H. & Abelson, J. (2000). *J. Mol. Biol.* **302**, 639–648.

Li, H., Trotta, C. R. & Abelson, J. (1998). *Science*, **280**, 279–284.

Lykke-Andersen, J., Aagaard, C., Semionenkov, M. & Garrett, R. A. (1997). *Trends Biochem. Sci.* **22**, 326–331.

Lykke-Andersen, J. & Garrett, R. A. (1997). *EMBO J.* **16**, 6290–6300.

Marck, C. & Grosjean, H. (2003). *RNA*, **9**, 1516–1531.

McRee, D. E. (1999). *J. Struct. Biol.* **125**, 156–165.

Moore, P. B. (1999). *Annu. Rev. Biochem.* **68**, 287–300.

Murshudov, G. N., Vagin, A. A., Lebedev, A., Wilson, K. S. & Dodson, E. J. (1999). *Acta Cryst.* D**55**, 247–255.

Navaza, J. (2001). *Acta Cryst.* D**57**, 1367–1372.

Otwinowski, Z. & Minor, W. (1997). *Methods Enzymol.* **276**, 307–326.

Perrakis, A., Harkiolaki, M., Wilson, K. S. & Lamzin, V. S. (2001). *Acta Cryst.* D**57**, 1445–1450.

Tang, T. H., Rozhdestvensky, T. S., d'Orval, B. C., Bortolin, M. L., Huber, H., Charpentier, B., Branlant, C., Bachellerie, J. P., Brosius, J. & Huttenhofer, A. (2002). *Nucleic Acids Res.* **30**, 921–930.

Trotta, C. R., Miao, F., Arn, E. A., Stevens, S. W., Ho, C. K., Rauhut, R. & Abelson, J. N. (1997). *Cell*, **89**, 849–858.